The mechanism of morphogenesis in a phase-separating concentrated multicomponent alloy

ZUGANG MAO[1], CHANTAL K. SUDBRACK[1], KEVIN E. YOON[1], GEORGES MARTIN[1,2] AND DAVID N. SEIDMAN[1,3]*

[1]Department of Materials Science and Engineering, Northwestern University, Evanston, Illinois 60208, USA
[2]Commissariat à l'Énergie Atomique, Cabinet du Haut Commissaire, Bâtiment Siège, 91191 Gif sur Yvette Cedex, France
[3]Northwestern University Centre for Atom-Probe Tomography, Northwestern University, Cook Hall, 2220 Campus Drive, Evanston, Illinois 60208, USA
*e-mail: d-seidman@northwestern.edu

What determines the morphology of a decomposing alloy? Besides the well-established effect of the nucleation barrier, we demonstrate that, in a concentrated multicomponent Ni(Al,Cr) alloy, the details of the diffusion mechanism strongly affect the kinetic pathway of precipitation. Our argument is based on the combined use of atomic-scale observations, using three-dimensional atom-probe tomography (3D APT), lattice kinetic Monte Carlo simulations and the theory of diffusion. By an optimized choice of thermodynamic and kinetic parameters, we first reproduce the 3D APT observations, in particular the early-stage transient occurrence of coagulated precipitates. We then modify the kinetic correlations among the atomic fluxes in the simulation, without altering the thermodynamic driving force for phase separation, by changing the vacancy–solute interactions, resulting in a suppression of coagulation. Such changes can only be quantitatively accounted for with non-zero values for the off-diagonal terms of the Onsager matrix, at variance with classical models.

Controlling the precipitation microstructure in alloys, by appropriate heat treatments, is at the core of metallurgical skill. With the achievement of atomic-scale resolution with direct observations, using three-dimensional atom-probe tomography (3D APT)[1–3], and with simulation, using lattice kinetic Monte Carlo (LKMC) techniques[4], it is now possible to study quantitatively the formation mechanism of the earliest stages of the precipitation microstructure. Provided that the diffusion mechanism is fully taken into account, LKMC enables an excellent simulation of the kinetic pathway for nucleation, growth and coarsening observed at the atomic scale by 3D APT in real alloys. This has been demonstrated[5–8] for the decomposition of a ternary Ni(Al,Cr) supersaturated solution, which is a model for more complex nickel-based superalloys. Recently, the combined use of 3D APT and LKMC has elucidated the origin of the 'core shell' structure of $Al_3(Sc,Zr)$ precipitates in Al, which is attributed to the details of the diffusion mechanism both in the supersaturated Al(Sc,Zr) solid solution and in $Al_3(Sc,Zr)$ (ref. 9).

On the basis of these successes, we address the still unanswered question of the influence of diffusional correlation effects[10] and vacancy properties on the nucleation, growth and coarsening pathway in concentrated alloys. In contrast to LKMC, the phenomenological descriptions of precipitation kinetics, for example, as used in DICTRA-type modelling[11], rely on two important simplifying assumptions that ignore the latter potential effects: the Onsager matrix is diagonal and vacancies are everywhere at equilibrium[12].

As shown by LKMC studies of dilute alloys, depending on the vacancy properties (that is, both the magnitude of vacancy–solute binding energies and the local composition dependence of the energy of the saddle-point configuration), solute atoms diffuse individually or as small clusters with various degrees of kinetic correlation. The potential importance of cluster migration was revealed by simulations of the ferromagnetic kinetic Ising model with conserved total spin, either with direct or vacancy-mediated exchange dynamics[13–15]. On the basis of a more realistic expression for the activation barrier for atom–vacancy exchange[16], several LKMC studies have revealed the impact of cluster migration on the kinetic pathway (for example, the existence of an incubation period) in phase-separating alloys[4,17–20].

How do the above conclusions relate to multicomponent alloys with high solubility limits, a situation where the concept of migrating clusters loses its physical significance? In concentrated solutions, we are left with phenomenological parameters (the matrix of Onsager coefficients, chemical potentials, diffusivity matrix), which encompass the atomistics of the alloy. We demonstrate how combined atomic-scale studies of the decomposition of a supersaturated Ni(Al,Cr) solution, using 3D APT observations and LKMC simulations, reveal the effects of flux coupling and correlation on the kinetic pathway for nucleation, growth and coarsening in a concentrated ternary Ni-base alloy, which is a model for complex superalloys.

DECOMPOSITION OF Ni(Al,Cr) SOLID SOLUTIONS

Solution-treated Ni-5.2 Al-14.2 Cr at.% alloys were quenched and then aged at 873 K for increasing amounts of time (2 min
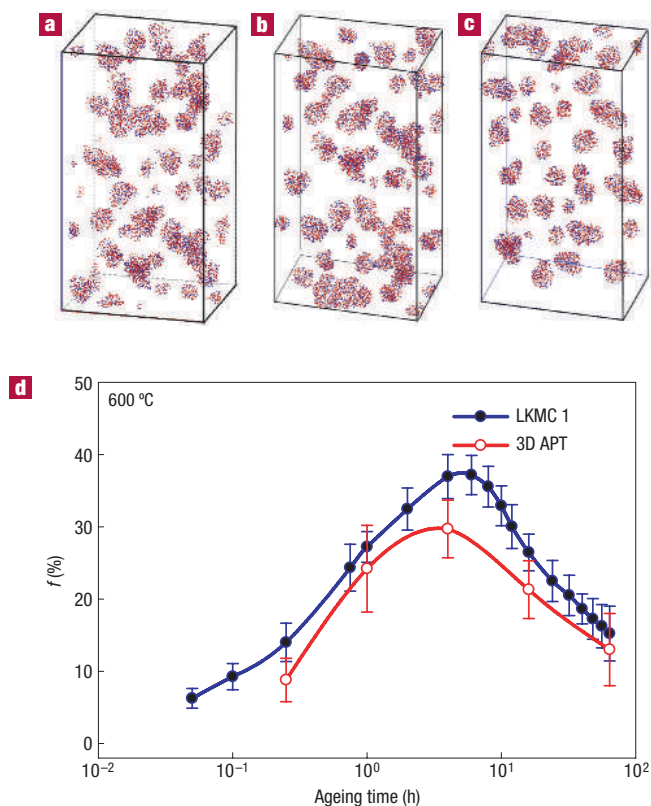
Figure 1 The morphology of γ'-precipitates, Ni$_3$(Al,Cr), in Ni 5.2 Al 14.2 Cr at.% after ageing at 873 K. **a**, As obtained from 3D APT experiments after 4 h. **b**, As simulated by LKMC with parameter set 1, see text. **c**, As simulated by LKMC with parameter set 2, see text. **d**, Fraction, f, of γ'-precipitates interconnected by necks as a function of ageing time, as observed with 3D APT and as simulated with parameter set 1. The colour coding of the atoms is as follows: chromium—blue; aluminium—red; and Ni atoms are omitted for clarity. The error bars are standard deviations of the mean.

Figure 2 The temporal evolution of γ'-precipitates in Ni 5.2 Al 14.2 Cr at.%. The γ'-precipitate volume fraction, ϕ, the number density, N_v, and mean radius, $\langle R \rangle$, as a function of ageing time at 873 K in Ni 5.2 Al 14.2 Cr at.%; as determined by 3D APT (red line) and as simulated in LKMC (blue line). Errors in experimental measurements of ϕ, N_v and $\langle R \rangle$ are based on precipitate number counts and errors associated with scaling the reconstructed volumes[7].

to 1,024 h) and analysed using 3D APT[1,2]. Typically, from 1.5×10^6 to several 10^6 atom positions are fully analysed using ADAM 1.5 (refs 21,22). Partial radial distribution functions were determined for all possible pair combinations for an as-quenched alloy and alloys aged for 2, 5 or 10 min. Isoconcentration (experimental data and simulation results) and iso-ordering (simulation results) surfaces are used to delineate γ' (L1$_2$) precipitates. Proximity histograms[23] are used to determine concentration profiles in the γ (face-centred-cubic, f.c.c.) matrix and in the γ' (L1$_2$) precipitates, relative to the γ/γ' heterophase interface[24,25].

From the 3D APT observations, we obtain the complete temporal evolution of the microstructure. In the as-quenched state, no γ'-precipitates are observed; the partial radial distribution functions indicate, however, small Ni–Al ordered domains, which evolve into Ni$_3$(Al$_{1-x}$Cr$_x$) precipitates, whose mean composition evolves continuously[26]. Nucleation occurs during the first hour, followed by a nucleation and growth regime (peaking at 4 h, with a γ'-precipitate number density $N_v = 3.2 \times 10^{24}$ m^{-3}), which is followed by a growth and coarsening regime, where the mean precipitate radius, $\langle R \rangle$, increases beyond 1 h as (time)$^{0.29\pm0.05}$. Concomitantly, the γ'-precipitate composition evolves slowly from Ni-19.1 Al-9.7 Cr at.% towards its equilibrium value, Ni-16.7 Al-6.8 Cr at.%; the latter is not quite achieved at 1,024 h. Both transmission electron microscopy and the stacking of {100} planes,

as revealed by 3D APT, demonstrate that the γ'-precipitates have the L1$_2$ structure[24].

A 3D APT experimental microstructure after four hours of ageing is shown in Fig. 1a. The Cr atoms are shown in blue and Al atoms in red; Ni is not shown for clarity. The striking feature demanding an atomistic explanation is the occurrence of γ'-precipitates interconnected by necks, with no evidence for anti-phase boundaries in the necks.

Interconnected γ'-precipitates are visible at as early as 15 min; their percentage, f, achieves a maximum value of $\approx30\%$ at 4 h (end of the nucleation and growth regime) and decays to about 2% at 256 h; at 1,024 h, f is not measurable with a conventional 3D APT, Fig. 1d.

LKMC SIMULATION OF THE DECOMPOSITION

The coherency strain in the present alloy is negligible, $0.06\pm0.04\%$ (refs 7,8), hence we proceed safely with rigid lattice LKMC simulations[4]. As coherent phase separation simply results from a succession of vacancy (v) jumps, the key ingredient of the simulation is the model for the exchange frequency, $W_{i,j}^{\alpha,v}$, between v on site j and an α atom on a nearest-neighbour site i. We choose $W_{i,j}^{\alpha,v} = \nu^\alpha \exp\left(-E_{i,j}^\alpha/kT\right)$, where ν^α is the attempt frequency, $E_{i,j}^\alpha$ is the energy change required to move the α atom
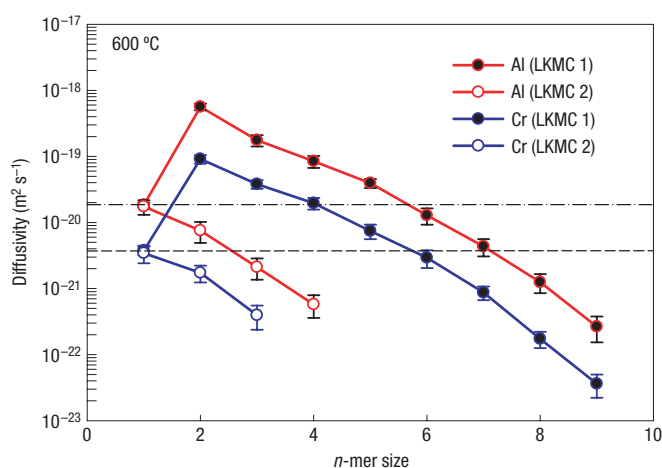
Figure 3 The significance of the diffusion of solute clusters (*n*-mers) in a Ni–Al or a Ni–Cr alloy. Diffusion coefficient (m² s⁻¹) of Al and Cr clusters (*n*-mers), as a function of the number of atoms (*n*) in the cluster: black dots for parameter set 1 and white dots for parameter set 2. The error bars are standard deviations of the mean.

from its initial stable position to the saddle-point position, k is Boltzmann's constant and T is the absolute temperature in degrees Kelvin. It is computed as the difference between two contributions: that of the jumping α atom to the saddle-point energy, $E^{\alpha}_{sp-i,j}$, and that of the α-vacancy pair to the energy of the initial stable configuration. As the cohesive energy is described as a sum of pair-wise interactions ($\varepsilon^{\alpha,\alpha'}_{i,i'}$ and $\varepsilon^{v,\alpha'}_{i,i'}$), this quantity is obtained by adding the contributions of all the bonds broken by the jump.

The full alloy thermodynamics, including vacancies as a constituent, is embodied in the values of $\varepsilon^{\alpha,\alpha'}_{i,i'}$ and $\varepsilon^{v,\alpha'}_{i,i'}$; the kinetics require additional parameters, specifically the values of v^{α} and $E^{\alpha}_{sp-i,j}$. Supplementary Information, Table S1 gives the values used; the technical details are in the Methods section.

The LKMC simulation results are in impressive agreement with the observed volume fraction of precipitates, $\phi(t)$, their number density, $N_v(t)$, and mean radius, $\langle R(t) \rangle$, values as a function of ageing time, up to 64 h, which is the maximum simulation time explored (Fig. 2). The measured compositions of the γ'-precipitates and γ-matrix are also in agreement (not shown) with the simulated values.

Strikingly, LKMC simulations also reproduce the γ'-precipitate morphologies observed with 3D APT (Fig. 1b and a, respectively).
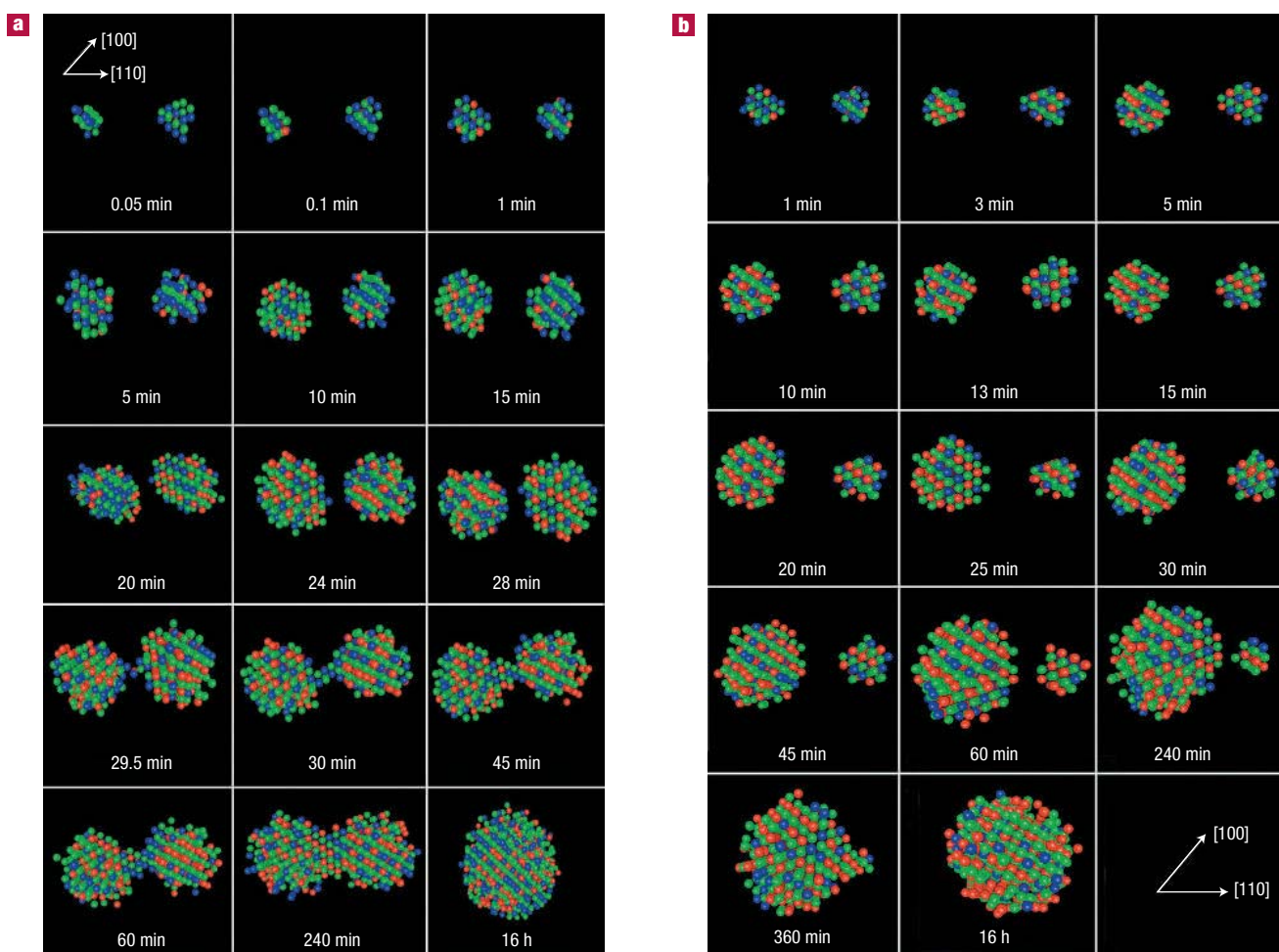
Figure 4 The effects of vacancy–solute binding energies on growth and coarsening of γ'-precipitates. a,b, Snapshots of the temporal evolution of two adjacent γ'-precipitates, as obtained using LKMC simulation with respectively parameter set 1, that is, with long-range vacancy–solute binding (**a**) and set 2, that is, omitting long-range vacancy–solute binding (**b**). The colour coding is as in Fig. 1a–c and Ni is green.

Table 1 The diffusion modes in LKMC 1 (with vacancy–solute binding) and LKMC 2 (without vacancy–solute binding): eigenvalues of the D matrix (m^2 s^{-1}) together with the components of the corresponding eigenvectors, C_{Ni}, C_{Al} and C_{Cr}. The norm of the eigenvector is equal to unity. The fast* mode is obtained by suppressing the off-diagonal terms of the Onsager matrix: note the inversion of the sign of the Ni component between parameter sets 1 and 1*.

Parameter set 1		
Eigenmode	Fast/fast*	Medium
D (m^2 s^{-1})	$(2.19 \pm 0.01)10^{-20}/(1.83 \pm 0.05)10^{-20}$	$(9.20 \pm 0.07)10^{-22}$
C_{Ni} (at. fr.)	$0.396 \pm 0.003/-0.043 \pm 0.002$	-0.75 ± 0.01
C_{Al} (at. fr.)	$0.842 \pm 0.005/0.996 \pm 0.004$	0.241 ± 0.009
C_{Cr} (at. fr.)	$0.367 \pm 0.003/0.074 \pm 0.005$	-0.615 ± 0.007
Parameter set 2		
Eigenmode	Fast/fast*	Medium
D (m^2 s^{-1})	$(3.2 \pm 0.3)10^{-21}/(3.6 \pm 0.8)10^{-21}$	$(1.3 \pm 0.1)10^{-21}$
C_{Ni} (at. fr.)	$0.023 \pm 0.002/-0.431 \pm 0.003$	0.92 ± 0.02
C_{Al} (at. fr.)	$0.967 \pm 0.007/0.897 \pm 0.005$	0.39 ± 0.01
C_{Cr} (at. fr.)	$0.255 \pm 0.004/0.104 \pm 0.004$	0.028 ± 0.008

The percentage of γ'-precipitates interconnected by necks evolves temporally in a manner similar to that observed by 3D APT, with semiquantitative agreement, Fig. 1d.

We also use LKMC to study the sensitivity of the temporal evolution of the microstructure to the diffusion mechanism, with fixed thermodynamics. The set of kinetic parameters used (attempt frequencies, energies of binding to the saddle point and vacancy–atom ghost interaction energies[27]) has the virtue of promoting fast diffusion for small solute clusters (n-mers) in elemental Ni, Fig. 3: this is a sign of strongly correlated diffusion. We can change the details of the vacancy-diffusion mechanism, without affecting the chemical potentials of the constituent elements (Ni, Al, Cr), by adjusting the vacancy–solute binding energy. To keep the order of magnitude of solute diffusion the same, we do not change the first neighbour vacancy–solute binding energy, but eliminate the vacancy–solute binding or anti-binding energies for farther shells, by setting for the latter, the vacancy–solute ghost interaction energy, equal to the Ni–solute interaction energy. The diffusivity of monomers is maintained by a slight readjustment of the attempt frequencies (see Supplementary Information, Table S1, Fig. 3). This corresponding set of parameters is denoted set 2 in the following, as opposed to set 1, which reproduces the experimentally observed kinetic pathway (Fig. 1b). Using the parameters of set 2, we observe that solute clusters (n-mers) are slower diffusers than monomers ($n = 1$) in elemental Ni (Fig. 3).

Simulating precipitation in the concentrated solid solution with the parameters of set 2 in LKMC suppresses the formation of necks (Fig. 1c). Figure 4a shows two adjacent γ'-precipitates during their evolution from 1 min to 16 h, using parameter set 1. Both γ'-precipitates grow with increasing time with their diameter ratio fluctuating around unity, with coagulation commencing between 29 and 30 min; a well-formed neck is visible at 45 min, which is the beginning of coalescence. Starting with the configuration at 1 min, we then simulate ageing with parameter set 2, Fig. 4b. The same pair of γ'-precipitates undergoes coarsening by an evaporation–condensation mechanism; although the two γ'-precipitates grow initially, the smaller one begins to shrink irreversibly beyond 15 min and evaporates after 240 min. Parameter set 2 thus generates the classical Lifshitz–Slyozov–Wagner (LSW) coarsening mechanism, which is either diffusion or interface-reaction controlled[28–30].

DIFFUSION AND THE NUCLEATION-GROWTH PATHWAY

Parameter sets 1 and 2 differ mainly in the vacancy–solute long-range binding energy. As the vacancy concentration in the LKMC simulation is vanishingly small, the simulated alloy should exhibit the same thermodynamics under parameter sets 1 and 2, but the diffusion matrix (D) must be different. This has been validated. In LKMC simulations, vacancies are conserved, as is the case in real alloys at the length scale pertinent to nucleation, which is significantly smaller than the mean distance between the dominant vacancy sources and sinks (dislocations)[31–33]. Consequently, the ternary Ni(Al,Cr) alloy is specified by four concentrations, C_{Ni}, C_{Al}, C_{Cr} and C_v, which sum to unity, three diffusion potentials, $(\mu_{Ni} - \mu_v)$, $(\mu_{Al} - \mu_v)$ and $(\mu_{Cr} - \mu_v)$, where μ_i is the chemical potential of Ni, Al or Cr and μ_v is that of the vacancy, and six Onsager coefficients, L_{NiNi}, L_{AlAl}, L_{CrCr}, L_{NiAl}, L_{NiCr} and L_{AlCr}. The flux of matter in the lattice frame of reference, $\mathbf{J}$, is given by

$$\mathbf{J} = -L\nabla\boldsymbol{\mu}(\Omega kT)^{-1} = -D\nabla\mathbf{C}\Omega^{-1}$$

where $\mathbf{J}$ is the column vector with elements J_{Ni}, J_{Al} and J_{Cr}, and similarly for the diffusion potentials and the concentrations

Table 2 Summary of the impact of vacancy–solute binding energies on the nucleation pathway and on diffusion.

Vacancy–solute binding	Active (parameter set 1)			Suppressed (parameter set 2)		
LKMC-simulated microstructure	Necks present (as observed by 3D atom–probe tomography)			No necks present		
Growth and coarsening mechanism	Coagulation–coalescence and Evaporation–condensation			Evaporation–condensation (no coagulation)		
Solute migration in pure solvent	Al and Cr clusters (n-mers) up to 5 times faster than monomers			Monomers faster than clusters (n-mers)		
	Ni	Al	Cr	Ni	Al	Cr
Fast diffusion eigenvector in the solid solution	0.47	1.00	0.44	0.02	1.00	0.26
$\delta\mathbf{C}$ (see text)	−0.35	1.00	−0.64	−0.35	1.00	−0.64
Width of concentration profile at 15 min at γ/γ' interfaces $\langle R \rangle = 0.75 \pm 0.14$ nm	Ni—1.7 nm (1.6 nm*) Al—1.6 nm (1.6 nm*) Cr—1.4 nm (1.3 nm*)			Ni—0.9 nm Al—1.1 nm Cr—1.0 nm		

* 3D APT results: see Fig. 5c for the experimental concentration profiles.

of atomic species; Ω is the atomic volume. The matrix D is given by the product of the Onsager matrix (L) and the susceptibility matrix:

$$D = \frac{L}{kT}\left(\frac{\partial(\mu_i - \mu_v)}{\partial C_j}\right)$$

with $i, j = $ Ni, Al, Cr. The off-diagonal terms in the three matrices have distinct physical origins: in L, the off-diagonal terms account for the kinetic coupling between fluxes, which results from the vacancy diffusion mechanism; in the susceptibility matrix, they account for the dependence of each chemical potential on the concentrations of all other elements. D combines both effects[10,34,35].

We have computed the elements of both matrices (Onsager and susceptibility) for parameter sets 1 and 2, using Monte Carlo techniques, in an equilibrium solid solution, whose composition is close to the terminal γ-solid-solution value expected after the completion of phase separation (Ni–3.4 Al–15.2 Cr at.%). L is calculated, following Einstein's definition, along an LKMC trajectory in the equilibrium solid solution[10]. The diffusion potentials are computed by the grand canonical Monte Carlo technique[36] applied to the quaternary solution—three chemical components plus vacancies. The susceptibility matrix is obtained by first computing the three diffusion potentials for five distinct compositions in the vicinity of the alloy's mean composition; we then carry out a multivariable linear regression versus composition changes. As expected, parameter sets 1 and 2 give the same thermodynamics for the solid solution ($\mu_{Al} - \mu_{Ni} = 0.165$ eV and $\mu_{Cr} - \mu_{Ni} = 0.144$ eV), but very different Onsager and susceptibility matrices. Once diagonalized, D reveals the dominant couplings between the fluxes of the three components: the eigenmodes are distinct for parameter sets 1 and 2, as shown in Table 1 and Supplementary Information, Fig. S1, where the eigenvectors have been normalized to unity.

With parameter set 1, the two faster modes differ by more than one order of magnitude; the slowest mode cannot be computed because of truncation error problems. Fast-1 mode is 20 times faster than fast-2 mode. During the first hour where nucleation proceeds, the root-mean-squared diffusion length, $2\sqrt{Dt}$, is ≈ 17 nm for the faster mode, ≈ 4 nm for the medium one, whereas the interprecipitate spacing is ≈ 8 nm (Fig. 2). Thus, morphogenesis is dominated by the faster mode. Fast* modes 1 and 2 in Table 1 correspond to diffusion matrices computed by imposing $L_{i\neq j} = 0$, that is, neglecting kinetic correlations in the flux coupling.

As seen in Supplementary Information, Fig. S1, the fast mode 1* is quite distinct from mode 1, and rather close to mode 2: by cancelling the long-range vacancy–solute binding energy, we have indeed decreased the kinetic correlations among the fluxes.

In this study, precipitates, whose equilibrium composition is 76.5 Ni–16.7 Al–6.8 Cr at.%, grow out of a 80.6 Ni–5.2 Al–14.2 Cr at.% solid solution. This process implies that Al diffuses to the precipitates, whereas Ni and Cr diffuse out of the precipitates. Such chemical exchanges are suggested in Supplementary Information, Fig. S1 by a unit vector $\delta\mathbf{C}$, whose components [−0.29 (Ni) +0.81 (Al) −0.52 (Cr)] are proportional to the difference of the equilibrium precipitate and matrix compositions. As is seen, depending on the parameter set, the coupling among fluxes favours or opposes the evolution required by equilibrium thermodynamics, as indicated by $\delta\mathbf{C}$ in Supplementary Information, Fig. S1. Indeed, under parameter set 1, the fast diffusion mode deviates more strongly from $\delta\mathbf{C}$ than under parameter set 2: the projections of the corresponding vectors on $\delta\mathbf{C}$ are 0.36 and 0.64, respectively.
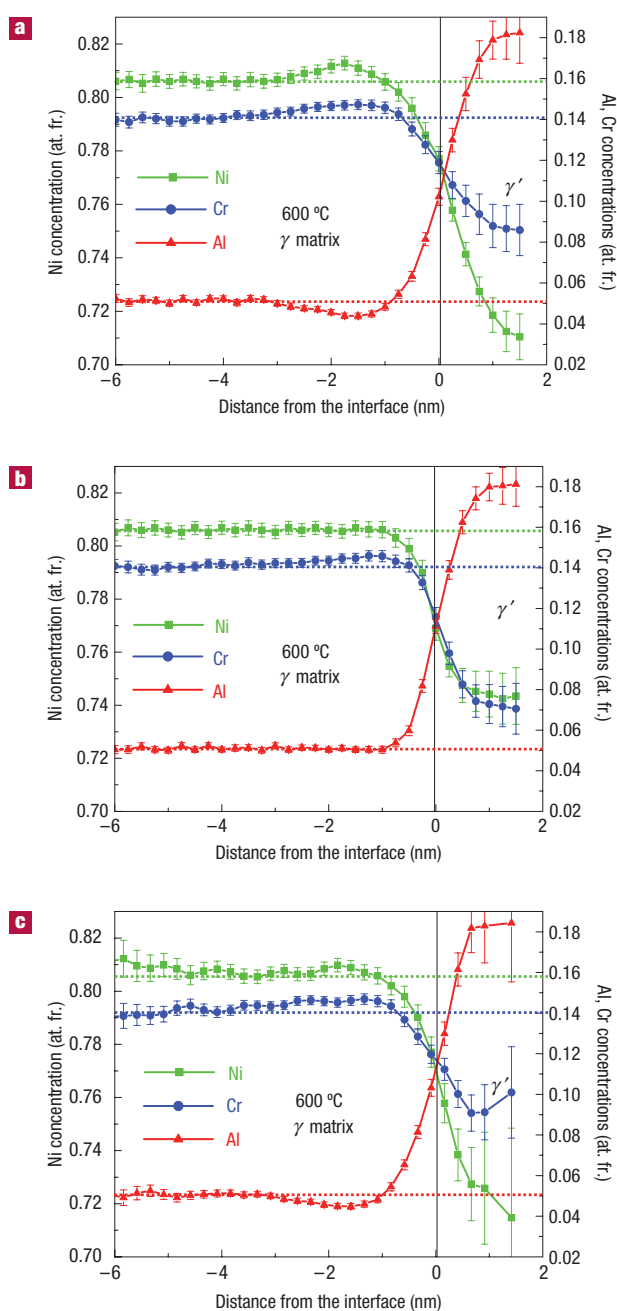
Figure 5 The effects of vacancy–solute binding energies on composition profiles associated with the γ/γ' interface. a–c, The Ni, Al and Cr concentration profiles as a function of distance from the γ/γ' iso-ordering interface when $\langle R \rangle$ achieves 0.75 ± 0.14 nm (the γ-solid-solution is on the left and the γ'-precipitate is on the right): parameter set 1, that is, with long-range vacancy–solute binding (**a**); parameter set 2, that is, omitting long-range vacancy–solute binding (**b**); experimental 3D APT concentration profiles (with respect to an isoconcentration surface) (**c**). For parameter set 1, note the Ni and Cr accumulation and Al depletion. These features vanish using parameter set 2 and the profiles are sharper. The experimental profiles are very similar to those generated by parameter set 1, with similar widths (Table 2). The error bars are standard deviations of the mean.

Such differences in couplings manifest themselves in the shapes of the concentration profiles as a function of distance to the γ'-precipitate/γ-matrix interface, integrating over all the

γ'-precipitates in the cell, using ADAM 1.5 (refs 21–23). In Fig. 5, the simulations are carried out for total ageing times such that the mean γ'-precipitate radius is similar for simulations with both sets 1 and 2, ≈ 0.7 nm, which is for 15 min. For the sake of clarity, in Table 2 we rescale the fast eigenvector, so that the Al component is $+1$. Under parameter set 1, which generates the LKMC kinetic pathway in agreement with the experimental one, an Al flux of amplitude 1 is accompanied by Ni and Cr fluxes with amplitudes of ≈ 0.47 and ≈ 0.44, respectively (the resulting vacancy flux is ≈ -1.91): the flow of Al to the γ'-precipitates opposes the outflow of Cr and Ni. As a consequence (Fig. 5a), the concentration profiles exhibit Ni and Cr accumulation and Al depletion in the vicinity of the precipitates. Under parameter set 2, the Al and Ni fluxes are almost decoupled (Ni/Al = 0.02)— the inflow of Al does not strongly oppose the outflow of Ni. It still opposes, however, the outflow of Cr but with a weaker strength compared with set 1 (Cr/Al = 0.26 versus 0.44). As a consequence (Fig. 5b), Ni accumulation and Al depletion are no longer noticeable, and Cr accumulation is much weaker. In addition, for parameter set 1, the Ni concentration profile extends deep into the solid solution (≈ 1.7 nm); it is significantly sharper (≈ 0.9 nm) for parameter set 2.

The 3D APT results (with $\langle R \rangle = 0.75 \pm 0.14$ nm, Fig. 5c), exhibit composition profiles similar to those shown in Fig. 5a, both in sharpness (Table 2) and shape. The depletion of Al and a slight accumulation of Ni and Cr in the experimental profile are consistent with the profiles in Fig. 5a.

As parameter sets 1 and 2 generate alloys with identical thermodynamics, the above change of interface sharpness is a direct consequence of the change in atomic mobilities. As a consequence, two adjacent γ'-precipitates interact, via the overlap of their associated diffusion fields, at a much larger distance when parameter set 1 is operating. As the concentration profiles observed at the interfaces are non-equilibrium ones, the γ'-precipitate/γ-matrix interfacial free energy is greater than that for fully equilibrated γ'-precipitates. The energy of the region of overlapping concentration profiles ('diffuse neck') can decrease by changing the concentration thereof into a well-formed neck. This is the reason why the coagulation–coalescence mechanism operates at early stages, when the γ'-precipitate number density, N_v, is large and the edge-to-edge distance between γ'-precipitates is small. It neither operates when N_v is small (later stages), nor when the precipitate–matrix interfaces are sharpened, by suppressing the long-range vacancy–solute binding energies (parameter set 2).

In summary, combining LKMC and diffusion theory, the coefficients of which are computed from LKMC, reveals the origin of the morphological features we observed in the 3D APT images of the phase-separating Ni(Al,Cr) alloy. The necking between adjacent precipitates, which occurs abundantly at early stages, results from the overlap of the diffusion fields around the γ'-precipitates; the latter are spread over distances much larger than an equilibrium interfacial thickness. This kinetic spreading results from a specific coupling between the diffusion fluxes of the alloy's constituents to and away from γ'-precipitates. All such effects disappear if the long-range solute–vacancy binding energies are artificially suppressed in LKMC. The latter energies do not contribute to the alloy's thermodynamics but strongly affect the kinetic couplings among fluxes. The modelling we use avoids the assumptions common to all the phenomenological models we are aware of, namely that the vacancies are permanently at local equilibrium ($\mu_v = 0$) and that the off-diagonal terms of the Onsager matrix can be neglected. These assumptions suppress the effects of vacancy–solute binding energies, which, as is demonstrated, is of key importance in selecting the kinetic pathway during the early stage of precipitation.

METHODS

LKMC SIMULATION METHOD

The values of $\varepsilon_{i,i'}^{\alpha,\alpha'}$ and $\varepsilon_{i,i'}^{\gamma,\alpha'}$ are deduced from a cluster expansion of the cohesive energy of Ni(Al,Cr) supercells computed from first principles, in the framework of density functional theory, local density approximation, combined with non-local, norm-conserving pseudopotentials, and plane-wave expansions, using the Cambridge Sequential Total Energy Package code[37]. The calculations use the band-by-band conjugate gradient technique to minimize the total energy with respect to plane-wave coefficients. In particular, the long-distance homo-atomic interactions are obtained using the Chen–Möbius inversion-lattice technique[38,39]. The values obtained (see Supplementary Information, Table S1) yield phase boundaries (solvus lines) in the Ni-rich portion of the calculated Ni–Al–Cr phase diagram at 1,023 K, in very good agreement with the generally accepted experimental diagram[40]. The ν^α and $E_{sp-i,j}^\alpha$ values in ref. 5 were used, which reproduce the impurity diffusion of Al and Cr in Ni to within 40–50% of the experimental diffusivities values.

Most LKMC simulations use a cell with 64^3 f.c.c. lattice cells with periodic boundary conditions, that is, 262,144 atomic sites, among which there is one vacant site; some simulations use 128^3 f.c.c. lattice cells (2,097,152 atomic sites). We use a residence-time algorithm to evaluate the physical time. The link with the experimental time is obtained by normalizing the LKMC time to the bulk equilibrium vacancy concentration in the Ni–Al–Cr alloy at 600 °C, which was calculated using 1.93 eV for the vacancy formation energy. As a precaution, it was verified that, using this procedure, the cell size has no effect on the kinetic pathway for a cell containing 4×10^6 or more atomic sites. The microstructures generated by the above LKMC simulations are analysed with ADAM 1.5 (refs 23–25).

References

1. Blavette, D. *et al*. The tomographic atom-probe—a quantitative 3-dimensional nanoanalytical instrument on an atomic-scale. *Rev. Sci. Instrum.* **64**, 2911–2919 (1993).
2. Cerezo, A., Godfrey, T. J., Sijbrandij, S. J., Smith, G. D. W. & Warren, P. J. Performance of an energy-compensated three-dimensional atom probe. *Rev. Sci. Instrum.* **69**, 49–58 (1998).
3. Kelly, T. F. *et al*. First data from a commercial local electrode atom probe (LEAP). *Microsc. Microanal.* **10**, 373–383 (2004).
4. Soisson, F., Barbu, A. & Martin, G. Monte Carlo simulations of copper precipitation in dilute iron-copper alloys during thermal ageing and under electron irradiation. *Acta Mater.* **44**, 3789–3800 (1996).
5. Pareige, C., Soisson, F., Martin, G. & Blavette, D. Ordering and phase separation in Ni-Cr-Al: Monte Carlo simulations versus three-dimensional atom probe. *Acta Mater.* **47**, 1889–1899 (1999).
6. Sudbrack, C. K. *et al*. in *Electron Microscopy: Its Role in Materials Research—The Mike Meshii Symposium* (eds Weertman, J. R., Fine, M. E., Faber, K. T., King, W. & Liaw, P.) 43–50 (TMS; The Minerals, Metals & Materials Society, Warrendale, PA, 2003).
7. Sudbrack, C. K., Yoon, K. E., Noebe, R. D. & Seidman, D. N. Temporal evolution of the nanostructure and phase compositions in a model Ni–Al–Cr alloy. *Acta Mater.* **54**, 3199–3210 (2006).
8. Sudbrack, C. K., Noebe, R. D. & Seidman, D. N. Compositional pathways and capillary effects during isothermal precipitation in a nondilute Ni–Al–Cr alloy. *Acta Mater.* **55**, 119–130 (2007).
9. Clouet, E. *et al*. Complex precipitation pathways in multicomponent alloys. *Nature Mater.* **5**, 482–488 (2006).
10. Allnatt, A. R. & Lidiard, A. B. *Atomic Transport in Solids* (Cambridge Univ. Press, Cambridge, 1993).
11. Andersson, J. & Ågren, J. Models for numerical treatment of multicomponent diffusion in simple phases. *J. Appl. Phys.* **72**, 1350–1355 (1992).
12. Thornton, K., Ågren, J. & Voorhees, P. W. Modelling the evolution of phase boundaries in solids at the meso- and nano-scales. *Acta Mater.* **51**, 5675–5710 (2003).
13. Binder, K. Applications of Monte Carlo methods to statistical physics. *Rep. Prog. Phys.* **60**, 487–559 (1997).
14. Fratzl, P. & Penrose, O. Kinetics of spinodal decomposition in the Ising model with vacancy diffusion. *Phys. Rev. B* **50**, 3477–3480 (1994).
15. Weinkamer, R. & Fratzl, P. By which mechanism does coarsening in phase separating alloys proceed? *Europhys. Lett.* **61**, 261–267 (2003).
16. Martin, G. Atomic mobility in Cahn's diffusion model. *Phys. Rev. B* **41**, 2279–2283 (1990).
17. Athénes, M., Bellon, P. & Martin, G. Effects of atomic mobilities on phase separation kinetics: A Monte Carlo study. *Acta Mater.* **48**, 3675–2688 (2000).
18. Le Bouar, Y. & Soisson, F. Kinetic pathways from EAM potentials: influence of the activation barriers. *Phys. Rev. B* **65**, 094103 (2002).
19. Rautiainen, T. T. & Sutton, A. P. Influence of the atomic diffusion mechanism on morphologies, kinetics, and the mechanisms of coarsening during phase separation. *Phys. Rev. B* **59**, 13681–13692 (1999).
20. Roussel, J. M. & Bellon, P. Vacancy-assisted phase separation with asymmetric atomic mobility: coarsening rates, precipitate composition, and morphology. *Phys. Rev. B* **63**, 184114 (2001).
21. Hellman, O. C., Blatz du Rivage, J. & Seidman, D. N. Efficient sampling for three-dimensional atom probe microscopy data. *Ultramicroscopy* **95**, 199–205 (2003).
22. Hellman, O. C., Vandenbroucke, J., Blatz du Rivage, J. & Seidman, D. N. Application software for data analysis for three-dimensional atom probe microscopy. *Mater. Sci. Eng. A* **327**, 29–33 (2002).
23. Hellman, O. C., Vandenbroucke, J. A., Rüsing, J., Isheim, D. & Seidman, D. N. Analysis of three-dimensional atom-probe data by the proximity histogram. *Microsc. Microanal.* **6**, 437–444 (2000).
24. Sudbrack, C. K. *Decomposition Behavior in Model Ni-Al-Cr-X Superalloys: Temporal Evolution and Compositional Pathways on a Nanoscale*. Thesis, Northwestern Univ. (2004) (http://arc.nucapt.northwestern.edu/refbase/show.php?record=16).

25. Yoon, K. E. *Temporal Evolution of the Chemistry and Nanostructure of Multicomponent Model Ni-based Superalloys*. Thesis, Northwestern Univ. (2004) (http://arc.nucapt.northwestern.edu/refbase/show.php?record=15).

26. Sudbrack, C. K., Noebe, R. D. & Seidman, D. N. Direct observations of nucleation in a nondilute multicomponent alloy. *Phys. Rev. B* **73**, 212101 (2006).

27. Doyama, M. & Koehler, J. S. The relation between the formation energy of a vacancy and the nearest neighbor interactions in pure metals and liquid metals. *Acta Metall.* **24**, 871–879 (1976).

28. Ardell, A. J. & Ozolins, V. Trans-interface diffusion-controlled coarsening. *Nature Mater.* **4**, 309–316 (2005).

29. Lifshitz, I. M. & Slyozov, V. V. The kinetics of precipitation from supersaturated solid solutions. *J. Phys. Chem. Solids* **19**, 35–50 (1961).

30. Wagner, C. Theorie der alterung von niederschlägen durch umlösen (Ostwald-reifung). *Z. Elektrochem.* **65**, 581–591 (1961).

31. Martin, G. & Desgranges, C. Diffusion in crystals with nonconservative defects. *Europhys. Lett.* **44**, 150–155 (1998).

32. Seidman, D. N. & Balluffi, R. W. in *Lattice Defects and their Interactions* (ed. Hasiguti, R. R.) 913–960 (Gordon-Breach, New York, 1968).

33. Svoboda, J., Fischer, F. D., Fratzl, P. & Kroupa, A. Diffusion in multi-component systems with no or dense sources and sinks for vacancies. *Acta Mater.* **50**, 1369–1381 (2002).

34. Hartmann, A., Weinkamer, R., Fratzl, P., Svoboda, J. & Fischer, F. D. Onsager's coefficients and diffusion laws—a Monte Carlo study. *Phil. Mag.* **85**, 1243–1260 (2005).

35. Barbe, V. & Nastar, M. A self-consistent mean field calculation of the phenomenological coefficients in a multi-component alloy with high jump frequency ratios. *Phil. Mag.* **86**, 1513–1538 (2006).

36. Foiles, S. M. & Adams, J. B. Thermodynamic properties of fcc transition metals as calculated with the embedded-atom method. *Phys. Rev. B* **40**, 5909–5915 (1989).

37. Payne, M., Teter, R., Allan, D., Arias, T. & Joannopoulos, J. Iterative minimization techniques for *ab initio* total-energy calculations: molecular dynamics and conjugate gradients. *Rev. Mod. Phys.* **64**, 1045–1097 (1992).

38. Chen, N., Chen, Z. & Wei, Y. Multidimensional inverse lattice problem and a uniformly sampled arithmetic Fourier transform. *Phys. Rev. E* **55**, R5–R8 (1997).

39. Liu, S., Li, M. & Chen, N. Möbius transform and inversion from cohesion to elastic constant. *J. Phys. Condens. Matter* **5**, 4381–4390 (1993).

40. Taylor, A. & Floyd, R. W. The constitution of nickel-rich alloys of the nickel-chromium-aluminum system. *J. Inst. Met.* **81**, 451–464 (1952–53).

Author contributions

Z.M. carried out the LKMC simulation; C.K.S. and K.E.Y. carried out the 3D APT experiments; D.N.S. supervised and mentored Z.M., C.K.S. and K.E.Y.; G.M. analysed the observations in terms of diffusion theory.

Competing financial interests

The authors declare that they have no competing financial interests.

Reprints and permission information is available online at http://npg.nature.com/reprintsandpermissions/

The mechanism of morphogenesis in a phase separating concentrated multi-component alloy

ZUGANG MAO[1], CHANTAL K. SUDBRACK[1], KEVIN E. YOON[1], GEORGES MARTIN[1,2]
AND DAVID N. SEIDMAN[1,3]

[1]Department of Materials Science and Engineering, Northwestern University,
Evanston, Illinois 60208, USA
[2]Commissariat à l'Énergie Atomique, Cabinet du Haut Commissaire,
Bâtiment Siège, 91191 Gif sur Yvette Cedex FRANCE
[3]Northwestern University Centre for Atom-Probe Tomography

(**Figure S1** and **Table S1**)

Figure Caption:

Figure S1:   Polar plot of the unit eigenvectors of the diffusion matrices (fast mode) under parameter sets 1 and 2 computed from the Onsager matrices either complete or truncated with the off-diagonal terms set to zero (1* and 2*). $\delta\mathbf{C}$ is a unit vector whose components scale with the composition difference between the precipitate and the matrix at equilibrium.

Fast mode

Ni

Al 0.0
Al 0.6
Al 0.8

1.0
0.8
0.6
0.4
0.2
0.0

1

2

Cr

-1.0 -0.8 -0.6 -0.4 -0.2 0.0 0.2 0.4 0.6 0.8 1.0

1*

-0.2
-0.4
-0.6
-0.8
-1.0

δC

2*

Al

1

2   1

0.8
0.6
0.4
0.2

Cr

Ni
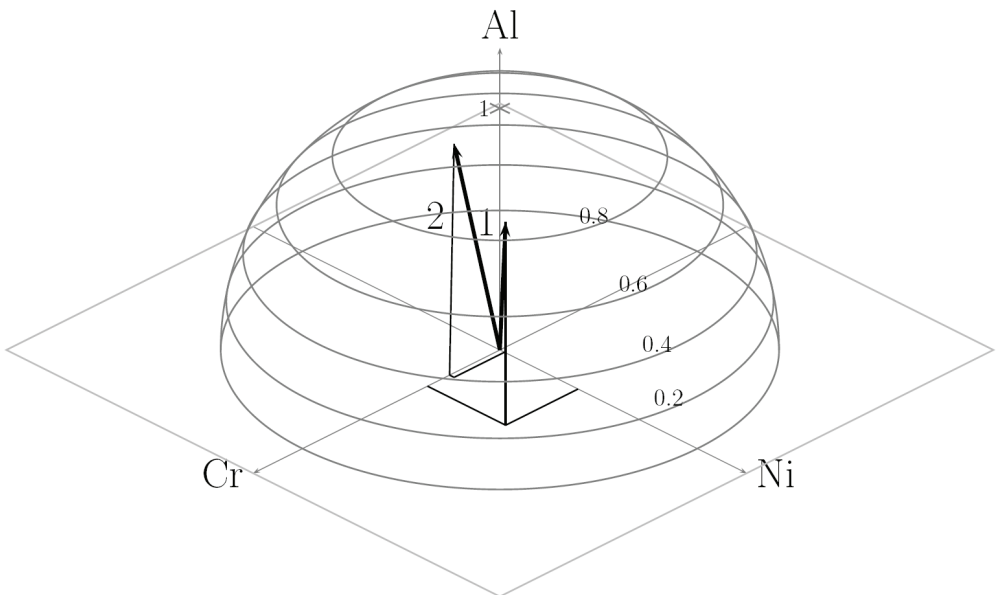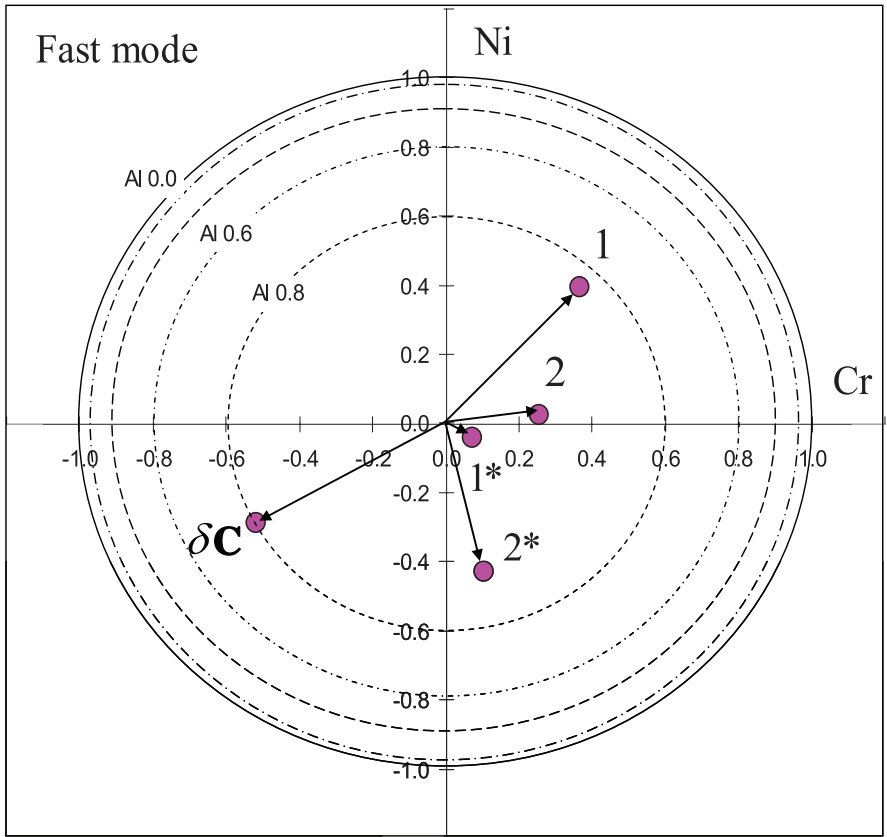
Table S1: (a) Pair interactions, up to fourth nearest-neighbour (NN), vacancy-solvent and vacancy-solute ghost interactions. (b) Kinetic parameters: binding energies to the saddle point $E^{\alpha}_{sp-i.j}$, attempt frequencies ν^{α}. All numbers are given, respectively, for parameter sets (1) and (2): see text.

(a)

$\varepsilon^{\alpha,\alpha'}$ (eV)	Ni-Ni	Al-Al	Cr-Cr	Ni-Al	Ni-Cr	Al-Cr	v-Ni (1)/(2)	v-Al (1)/(2)	v-Cr (1)/(2)
1st NN	-0.7485	-0.5786	-0.6845	-0.7495	-0.7582	-0.6963	-0.178	-0.221	-0.223
2nd NN	-0.0135	-0.0265	-0.0112	0.0349	0.0257	0.0225	0/ $\varepsilon^{Ni,Ni}$	0/ $\varepsilon^{Al,Ni}$	0/ $\varepsilon^{Cr,Ni}$
3rd NN	0.0142	0.0084	-0.0185	-0.0285	0.00526	0.0211	0/ $\varepsilon^{Ni,Ni}$	0/ $\varepsilon^{Al,Ni}$	0/ $\varepsilon^{Cr,Ni}$
4th NN	-0.00664	-0.0121	-0.00945	0.0125	-0.0166	0.115	0/ $\varepsilon^{Ni,Ni}$	0/ $\varepsilon^{Al,Ni}$	0/ $\varepsilon^{Cr,Ni}$

(b)

	Ni	Al	Cr
$E^{\alpha}_{sp-i.j}$ (eV)	-9.750	-9.412	-9.862
ν^{α} (s^{-1}) (1)/(2)	$1.10 \times 10^{15}/1.28 \times 10^{15}$	$1.10 \times 10^{15}/2.26 \times 10^{15}$	$8.7 \times 10^{14}/1.84 \times 10^{15}$